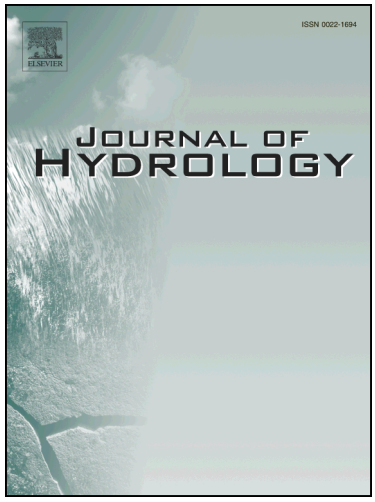

A comprehensive numerical analysis of the hydraulic behavior of a permeable pavement

Giuseppe Brunetti, Jiř í Šimůnek, Patrizia Piro

PII: S0022-1694(16)30460-7
DOI: http://dx.doi.org/10.1016/j.jhydrol.2016.07.030
Reference: HYDROL 21416

To appear in: *Journal of Hydrology*

Received Date: 2 March 2016
Revised Date: 1 July 2016
Accepted Date: 18 July 2016

Please cite this article as: Brunetti, G., Šimůnek, J., Piro, P., A comprehensive numerical analysis of the hydraulic behavior of a permeable pavement, *Journal of Hydrology* (2016), doi: http://dx.doi.org/10.1016/j.jhydrol.2016.07.030

A comprehensive numerical analysis of the hydraulic behavior of a permeable pavement

Giuseppe Brunetti[a*], Jiří Šimůnek[b], and Patrizia Piro[a]

[a] *Department of Civil Engineering, University of Calabria, Rende, CS 87036, Italy*

[b] *Department of Environmental Sciences, University of California, Riverside, CA 92521, USA*

[*]Corresponding author: giusep.bru@gmail.com

ABSTRACT

The increasing frequency of flooding events in urban catchments related to an increase in impervious surfaces highlights the inadequacy of traditional urban drainage systems. Low Impact Development (LID) techniques have proven to be a viable and effective alternative by reducing stormwater runoff and increasing the infiltration and evapotranspiration capacity of urban areas. However, the lack of adequate modeling tools represents a barrier in designing and constructing such systems. This paper investigates the suitability of a mechanistic model, HYDRUS-1D, to correctly describe the hydraulic behavior of permeable pavement installed at the University of Calabria. Two different scenarios of describing the hydraulic behavior of the permeable pavement system were analyzed: the first one uses a single-porosity model for all layers of the permeable pavement; the second one uses a dual-porosity model for the base and sub-base layers. Measured and modeled month-long hydrographs were compared using the Nash-Sutcliffe efficiency (*NSE*) index. A Global Sensitivity Analysis (GSA) followed by a Monte Carlo filtering highlighted the influence of the wear layer on the hydraulic behavior of the pavement and identified the ranges of parameters generating *behavioral* solutions. Reduced ranges were then used in the calibration procedure conducted with the metaheuristic Particle swarm optimization (PSO) algorithm for the estimation of hydraulic parameters. The best fit value for the first scenario was *NSE* = 0.43; for the second scenario, it was *NSE* = 0.81, indicating that the dual-porosity approach is more appropriate for describing the variably-saturated flow in the base and sub-base layers. Estimated parameters were validated using an independent, month-long set of measurements, resulting in *NSE* values of

0.43 and 0.86 for the first and second scenarios, respectively. The improvement in correspondence between measured and modeled hydrographs confirmed the reliability of the combination of GSA and PSO in dealing with highly dimensional optimization problems. Obtained results have demonstrated that PSO, due to its easiness of implementation and effectiveness, can represent a new and viable alternative to traditional optimization algorithms for the inverse estimation of unsaturated hydraulic properties. Finally, the results confirmed the suitability and the accuracy of HYDRUS-1D in correctly describing the hydraulic behavior of permeable pavements.

Keywords: permeable pavement; urban drainage; infiltration; sensitivity analysis; global optimization; particle swarm

Table of Contents

INTRODUCTION

Progressing urbanization, connected with the demographic growth of the last decades, has led to an increase in impervious surfaces in urban catchments at the expense of natural areas. This long-term process has resulted in the alteration of the natural hydrological cycle by reducing the infiltration and evaporation capacity of urban catchments, increasing surface runoff, and reducing groundwater recharge. While some studies highlighted a decrease of recharge as a result of an increase of impervious surfaces, other studies identified an increase in recharge due to the leakage of water from an urban infrastructure, such as sewer and water supply systems. The effect of urbanization on groundwater recharge is discussed in detail by Price (2011).

Another important factor is that the frequency of extreme rainfall events, characterized by high intensity and short duration, is expected to increase in the near future as a consequence of climate change (Kundzewicz et al., 2006; Min et al., 2011). For example, a recent study of Wasko and Sharma (2015) identified a strong correlation between intense precipitation peaks and high temperatures. They concluded that the expected global warming could lead to an increase of short-duration floods. The correlation between atmospheric temperature and extreme rainfall intensities was also confirmed in other studies (e.g., Westra et al., 2014). This will be accompanied by a more frequent occurrence of flooding events in urban areas (Carbone et al., 2015b).

The traditional approach to urban drainage systems focuses on collecting stormwater in piped networks and transporting it off-site as quickly as possible. The increasing frequency of flooding events proves that a new design paradigm for drainage systems is needed. This approach must aim to restore the natural hydrological cycle of urban catchments by increasing their evapotranspiration and infiltration capacity. In recent years, Low Impact Development (LID), an innovative approach to land development, has gained increasing popularity. LID is a 'green' approach for stormwater management that seeks to mimic the natural hydrology of a site using decentralized micro-scale control measures (Coffman, 2002). LID practices consist of bioretention cells, infiltration wells/trenches, stormwater wetlands, wet ponds, level spreaders, permeable

pavements, swales, green roofs, vegetated filter/buffer strips, sand filters, smaller culverts, and water harvesting systems. Several studies have evaluated the benefits of LIDs. For example, Newcomer et al. (2014) used a numerical model to demonstrate the benefits of LIDs, in particular of an infiltration trench, on recharge and local groundwater resources for future climate scenarios. In another paper, Berardi et al. (2014) demonstrated how green roofs may contribute to the development of more sustainable buildings and cities. Environmental benefits included ecological preservation, mitigation of air and water pollution, enhancement of urban hydrology, a decrease of urban heat island effects, a reduction of energy consumption, etc. Furthermore, green roofs were able to significantly reduce storm-water runoff and retain rainfall volume with retention efficiencies ranging from 40% to 80% (Bengtsson et al., 2004); bioretention cells were shown to reduce average peak flows by at least 45% during a series of rainfall events in Maryland and North Carolina (Davis, 2008). Even though the results of available studies are encouraging, more research is needed to precisely assess the impact of LIDs on the hydrological cycle.

Most impervious surfaces in urban catchments consists of roofs, roads, parking lots and road shoulders. The development of any large impervious surface commonly leads to multiple impacts on stream systems. These impacts include higher peak stream flows, which cause channel incision, bank erosion, and increased sediment transport (Trimble, 1997; Whipple et al., 1981). Another consequence of these impervious surfaces is the reduction of infiltration, which lowers groundwater recharge (Rose and Peters, 2001) and potentially also stream base flow (DeWalle et al., 2000; Simmons and Reynolds, 1982). Permeable pavements represent one solution to the problem of increased stormwater runoff and decreased stream water quality. They consist of a surface concrete layer, a filter layer made of sand and other materials, a stony base, and sub-base layers. Permeable pavements offer great advantages in terms of runoff reduction (Collins et al., 2008), water retention, and water quality (Brattebo and Booth, 2003).

In spite of many well-known benefits of permeable pavements and other LID practices, the transition to sustainable urban drainage systems is very slow. One of the key limiting factors in the

widespread adoption of such systems is the lack of adequate analytical and modeling tools (Elliot and Trowsdale, 2007). The availability of an effective LID modeling software could encourage a wider adoption of LID principles. Although several stormwater models can be applied to the LID analysis (Elliot and Trowsdale, 2007), most of them do not incorporate accurate descriptions of hydrological processes involved, which leads to inaccurate predictions. Moreover, existing tools do not incorporate automatic parameter optimization techniques and sensitivity analysis routines, which have proven to be fundamental when the model includes multiple parameters. In recent years, researchers have focused their attention on applying and developing physically-based models for the LID analysis (Carbone et al., 2015a), however more research is still needed in this direction.

For example, the HYDRUS software suite (Šimůnek et al., 2008) has been widely used in the literature for the description of the hydraulic behavior of green roofs (Hilten et al., 2008; Li and Babcock, 2015; Newcomer et al., 2014; Palla et al., 2009), with excellent agreement between numerical simulations and experimental data. Newcomer et al. (2014) investigated the effects of LIDs on recharge. In their study, the HYDRUS-2D software was used to simulate flow from an infiltration trench and an irrigated lawn installed at the San Francisco State University. While the model was calibrated by comparing the simulated and measured recharge, only few details were given about the calibration procedure. The calibrated model was then used to simulate the behavior of LIDs for future precipitation scenarios. Hilten et al. (2008) used HYDRUS-1D to study the effectiveness of green roofs in mitigating stormwater. Simulations were run using HYDRUS-1D for a 24-h design storm to determine peak flow, retention, and detention time for runoff. Li and Babcock (2015) used HYDRUS-2D to model the hydrologic response of a pilot green roof system. The root-mean-square error deviation (RMSD) between the modeled water contents and field measurements ranged between 0.38 and 1.74%. This suggests that the use of mechanistic models, such as HYDRUS, represents one of the most valuable alternatives to empirical and conceptual models for the LID analysis.

Among all LID practices, permeable pavements are those that lack modeling tools able to describe their hydraulic behavior most. The heterogeneity of materials that compose a permeable pavement, together with the high infiltration rates (Brattebo and Booth, 2003), which may lead to preferential flow and especially in the base and sub-base layers, pose complex problems in the numerical modeling of these systems. Very few modeling tools exist in the literature for permeable pavements. One of them is included in the Storm Water Management Model (SWMM) (Gironás et al., 2010). However, results obtained by SWMM have proven to be inaccurate, especially in the description of the effects of base and sub-base layers on the infiltration processes (Zhang and Guo, 2015). HYDRUS has also been used for the description of variably-saturated flow in permeable pavements. Illgen et al. (2007) used HYDRUS-2D for the numerical analysis of a permeable pavement and calibrated the model against experimental data collected at a laboratory test facility. The calibrated model was then used to simulate different scenarios not investigated during the laboratory campaign. The Illgen et al. (2007) study provided only limited details about the calibration of soil hydraulic parameters and their uncertainty and sensitivity. The occurrence of preferential flow in the permeable pavement was also not investigated. Moreover, the model was used to simulate a laboratory test facility, the behavior of which can differ from a field scale experimental facility. On the other hand, Carbone et al. (2014) used HYDRUS-1D to model a permeable pavement at the field scale. The HYDRUS-1D model was calibrated against four different rainfall events with optimal results. In this study, the permeable pavement was modeled as a single homogeneous layer and the differences between hydraulic properties of different layers were neglected. Furthermore, the numerical simulations were event-based. In both studies, calibration of soil hydraulic properties was carried out manually without taking advantage of more recent global optimization algorithms. This indicates that research in this direction is limited, with only inconclusive results that need to be further investigated.

The lack of studies that provide a comprehensive description of the hydraulic behavior of a permeable pavement at the field scale and that propose a general methodology for the estimation of

its hydraulic parameters suggests that research is particularly needed in the development and identification of accurate modeling tools for the analysis of LID practices, especially for permeable pavements. The aim of this study is to investigate the suitability of the HYDRUS mechanistic model to correctly describe unsaturated flow in typical permeable pavement, installed at the experimental site of the University of Calabria. Multiple uniform and nonequilibrium flow models included in HYDRUS-1D, such as single- and dual-porosity models, are used to describe the hydraulic behavior of the permeable pavement. The problem is addressed in the following way. First, a Global Sensitivity Analysis (GSA) is carried out to prioritize hydraulic parameters and identify those that are non-influential. Results of the GSA, combined with a Monte Carlo filtering approach, are used to investigate the parameter space and identify *behavioral* regions. These regions are then used in the calibration process conducted with the Particle Swarm Optimization (PSO) algorithm. The use of PSO for the determination of unsaturated hydraulic properties represents a new important application of this method. Finally, the calibrated model is validated on an independent set of measurements.

MATERIALS AND METHODS

Site Description

The University of Calabria is located in the south of Italy, in the vicinity of Cosenza (39°18′ N 16°15′ E). The climate is Mediterranean with a mean annual temperature of 15.5 °C and an average annual precipitation of 881.2 mm. The permeable pavement is part of the "Urban Hydraulic Park," which also includes an extensive green roof, a bioretention system, and a sedimentation tank connected with a treatment unit. The permeable pavement has an area of 154 m^2, an average slope of 2%, and a total depth of the profile of 0.98 m. Figure 1 shows a schematic of the permeable pavement, consisting of 5 layers.

193 The surface wear layer consists of porous concrete blocks characterized by high
194 permeability. Base, sub-base and bedding layers were constructed by following the suggestions of
195 the Interlocking Concrete Pavement Institute (ICPI), which recommends certain ASTM stone
196 gradations. The ASTM numbers and corresponding gradations can be found in ASTM D 448,
197 *Standard Classification for Sizes of Aggregate for Road and Bridge Construction*. The ASTM
198 N°57, used for the base layer, is characterized by a porosity of about 30-35%. The ASTM N°2 is
199 used in the sub-base layer for its stability and a high volumetric porosity of about 40%. The ASTM
200 N°8 is used for the bedding layer and the protection layer and has a porosity of about 20% of
201 volume. The bedding layer is composed of a mixture of sand, glass sand, and zeolite to improve the
202 pollutant removal efficiency of the permeable pavement for typical contaminants of stormwater
203 runoff. A high permeability geotextile with a fiber area weight of 60 g/m^2 is placed at the interface
204 between the bedding layer and the base layer to prevent sand from migrating into the bottom layers.
205 An impervious membrane is placed at the bottom of the profile to prevent water from percolating
206 into deeper horizons. The protection layer which is composed of coarse sand is placed between the
207 sub-base layer and the impervious membrane. The baseflow is collected in a horizontal drain, which
208 consists of a perforated PVC pipe, and is conducted to a manhole for quantity and quality
209 measurements.

210 A weather station located directly at the site measures precipitation, wind velocity and
211 direction, air humidity, air temperature, atmospheric pressure, and global solar radiation. Rain data
212 are measured by a tipping bucket rain gauge with a resolution of 0.254 mm and an acquisition
213 frequency of one minute. Climatic data are acquired with a frequency of five minutes. Data are
214 processed and stored in the SQL database.

215 Two flux meters, composed of a PVC pipe with a sharp-crested weir and a pressure
216 transducer, measure baseflow and runoff from the permeable pavement. The pressure transducer
217 (Ge Druck PTX1830) measures the water level inside the PVC pipe and has a range of
218 measurement of 75 cm with an accuracy of 0.1 % of the full scale. The pressure transducers were

219 calibrated in the laboratory by using a hydrostatic water column, linking the electric current
220 intensity with the water level inside the column. The exponential head-discharge equations for the
221 two PVC flux meters were obtained by fitting the experimental data with a coefficient of
222 determination R^2=0.999 for both devices. Runoff and baseflow data were acquired with a time
223 resolution of 1 minute and stored in the SQL database. No measurements of pressure heads or
224 volumetric water contents inside the pavement were taken.

225 Two month-long data sets were selected for further analysis (Fig. 2). The first data set,
226 which started on 2014-01-15 and ended on 2014-02-15, was used for parameter optimization and
227 sensitivity analysis. Total precipitation and total potential evapotranspiration for the first data set
228 were 274 mm and 43 mm, respectively. The second data set, which started on 2014-03-01 and
229 ended on 2014-03-31, was used for model validation. Total precipitation and total potential
230 evapotranspiration for the second data set were 175 mm and 81 mm, respectively. The second data
231 set was selected so that it had significantly different meteorological data than during the first period.
232 The optimization set is characterized by multiple rain events with few dry periods. The validation
233 set has fewer rain events, which are concentrated at the beginning and end of the time period and
234 separated by a relatively long dry period between. Surface runoff was not observed during these
235 time periods.

236 Potential evaporation was calculated using the Penman-Monteith equation (Allen et al.,
237 1998). The permeable pavement was installed in 2013 and has been constantly exposed to
238 atmospheric conditions and traffic since then that has altered the surface roughness and color. For
239 these reasons, an albedo of 0.25 was used as suggested by Levinson and Akbari (2002) for
240 weathered gray cement.

241

242 ***Theory***

243 Water flow simulations were conducted using the HYDRUS-1D software (Šimůnek et al.,
244 2008). HYDRUS-1D is a one-dimensional finite element model for simulating the movement of

245 water, heat, and multiple solutes in variably-saturated porous media. HYDRUS-1D implements
246 multiple uniform (single-porosity) and nonequilibrium (dual-porosity and dual-permeability) water
247 flow models (Šimůnek and van Genuchten, 2008). In this study, two different conceptual models
248 were used to represent flow in the permeable pavement (Table 1).

249 Scenario I assumed that water flow in all five soil layers of the permeable pavement can be
250 described using the classical single-porosity approach (SPM). Unsaturated water flow is then
251 described using the one-dimensional Richards equation:

252 $$\frac{\partial \theta}{\partial z} = \frac{\partial}{\partial z}\left[K(h)\left(\frac{\partial h}{\partial z} + 1\right)\right] \quad (1)$$

253 where θ is the volumetric water content [-], h is the soil water pressure head [L], $K(h)$ is the
254 unsaturated hydraulic conductivity [LT^{-1}], t is time [T], and z is the soil depth [L]. The soil
255 hydraulic properties are described by the van Genuchten – Mualem relation (van Genuchten, 1980):

256 $$\theta = \begin{cases} \dfrac{\theta_s - \theta_r}{(1 + (\alpha|h|)^n)^m} + \theta_r & \text{if } h \le 0 \\ \theta_s & \text{if } h > 0 \end{cases} \quad (2)$$

257 $$S_e = \frac{\theta - \theta_r}{\theta_s - \theta_r}$$

258 $$K = \begin{cases} K_s S_e^L \left[(1 - (1 - S_e^{\frac{1}{m}})^m \right]^2 & if\ h \le 0 \\ K_s & if\ h > 0 \end{cases} \quad (3)$$

259 $$m = 1 - \frac{1}{n}$$

260 where θ_r [-] is the residual water content, θ_s [-] is the saturated water content, K_s [LT^{-1}] is the
261 saturated hydraulic conductivity, n is a pore-size distribution index [-], α is a parameter related to
262 the inverse of the air-entry pressure [L^{-1}], L indicates the tortuosity and is usually assumed to be 0.5
263 for many soils, and S_e is the effective saturation [-]. In order to simplify the model (to lower the
264 number of unknown parameters), the residual water content of all layers was fixed. In particular, the

265 residual water content for the wear and bedding layers was assumed to be 0.045 and 0.03,
266 respectively, while the residual water content for both the base and sub-base layers was assumed to
267 be 0.0, considering that they were composed of crushed stones. Furthermore, considering that the
268 bedding layer and the protection layer had the same stone gradation, ASTM N°8, the same set of
269 parameters was used for both. Despite of all these considerations, this scenario still involves 16
270 parameters (θ_s, α, n, and K_s for 4 soil layers).

271 Scenario II assumes a single-porosity model for the wear layer, the bedding layer, and the
272 protection layer, and a dual-porosity model for the base and sub-base layers. This configuration was
273 selected in order to consider the occurrence of preferential flow in the coarse layers of the
274 pavement.

275 The base and sub-base layers are composed of crushed stones, with particle size diameters
276 ranging from 2.5 to 37 mm in the base layer and from 20 to 75 mm in the sub-base layer. Crushed
277 stones were washed before installation in order to remove fine particles. This narrow gradation
278 provides a high volume of voids and increases the water storage and infiltration capacities of these
279 two layers. From a physical point of view, the structure of the base and sub-base materials closely
280 resembles fractured aquifers (Barenblatt et al., 1960). Fractured aquifers are represented by a blocky
281 matrix system intercepted by fractures. Open and well-connected fractures represent high
282 permeability pathways that are many orders of magnitude more permeable than the porous rock
283 matrix. At the same time, one of the characteristics of a fractured aquifer is that the fractures occupy
284 a much smaller volume than the pores of the rock matrix. Traditionally, fractured porous media are
285 thus represented by two separate flow domains: the high permeability (mobile) domain, the network
286 of connected fractures characterized by advective flow, and the low permeability (immobile)
287 domain, dominated by diffusion. The rock matrix also provides storage capacity because of its
288 significantly larger volume than the fracture system. Typical breakthrough curves for a fractured
289 aquifer are characterized by early breakthrough and long tailing (Geiger et al., 2010). This is due to
290 the fact that the matrix has a delayed response to pressure head changes that occur in the

surrounding fractures. The resulting pressure difference induces matrix-fracture interflow. This flow takes place after initial fracture flow and before the matrix and fracture pressures equilibrate (Bai et al., 1994). Several studies have demonstrated the long tailing from permeable pavements in discharge hydrographs (e.g., Brattebo and Booth, 2003; Fassman and Blackbourn, 2010) and attributed this effect to the storage and flow through the base and sub-base layers.

The classical approach to model water flow in fractured porous media is the so-called "dual-porosity" or "mobile-immobile water" (MIM) approach (Barenblatt et al., 1960; van Genuchten and Wierenga, 1976; Warren and Root, 1963). This approach assumes that flow occurs only in the mobile fracture domain, for which an effective permeability must be known, while water in the matrix domain is immobile. Both domains are connected by a simple first-order transfer function, which accounts for the exchange of fluid across the boundary of the two domains.

In the dual-porosity approach, the liquid phase is divided into two domains:

$$\theta = \theta_f + \theta_m \tag{4}$$

where subscript *f* refers to the (mobile) fracture system, and subscript *m* refers to the immobile matrix domain. The dual-porosity water flow formulation is based on a modified Richards equation for flow in fractures and a mass balance equation for moisture dynamics in the matrix:

$$\frac{\partial \theta_f}{\partial z} = \frac{\partial}{\partial z}\left[K(h)\left(\frac{\partial h}{\partial z}+1\right)\right] - \Gamma_w \tag{5}$$

$$\frac{\partial \theta_m}{\partial t} = \Gamma_w \tag{6}$$

where Γ_w is the mass transfer between two domains, which is assumed to be proportional to the difference in effective saturations of the two regions (Šimůnek and van Genuchten, 2008; Simunek et al., 2003):

$$\Gamma_w = \omega \cdot (S_e^m - S_e^{im}) \tag{7}$$

where ω is a first-order coefficient [T^{-1}]. Compared to assuming a pressure head based driving force for the mass transfer, the dual-porosity model based on (7) requires significantly less parameters

since one does not need to know the retention function (and corresponding parameters) for the matrix region explicitly, but only its residual and saturated water contents (Simunek et al., 2003). The residual water content for the mobile domain of both the base and sub-base layers is assumed to be 0.0 (Simunek et al., 2003). The tortuosity factor, L, is again assumed to be 0.5 for all layers. Scenario II thus includes 20 parameters (additionally also ω and θ_s of the immobile domain for the base and subbase layers).

Numerical Domain and Boundary Conditions

The numerical domain representing the stratigraphy of the permeable pavement was divided in 5 layers. The bedding layer and the protection layer had the same properties since they were constructed using the same ASTM N^{o}8 stone gradation. A relatively fine, finite element mesh with a constant element size of 0.5 cm was used in order to minimize mass balance errors and avoid non-convergent runs during sensitivity analysis and parameter optimization. An atmospheric boundary condition was applied at the pavement surface using (a) precipitation and potential evaporation fluxes, (b) a prescribed zero pressure head (saturation) during ponding, and (c) equilibrium between the pavement surface water content and atmospheric water vapor when atmospheric evaporative demand could not be met by the wear layer. A seepage face boundary condition was specified at the bottom of the protection layer. A seepage face boundary acts as a zero pressure head boundary when the bottom boundary node is saturated and as a no-flux boundary when it is unsaturated. The initial conditions were specified in terms of the soil water pressure head and were set to linearly increase with depth, from -90 cm at the top of the flow domain (z = 0) to -0.5 cm at the bottom (z = -98). The surface layers are assumed to be drier than the bottom layers since they are directly exposed to evaporation.

Objective Function

The Nash-Sutcliffe Efficiency (NSE) index (Nash and Sutcliffe, 1970) is used for evaluating the agreement between hydrographs:

$$NSE = 1 - \left[\frac{\sum_{i=1}^{T} (Q_i^{obs} - Q_i^{\mathrm{mod}})^2}{\sum_{i=1}^{T} (Q_i^{obs} - Q_{mean}^{obs})^2} \right] \quad (8)$$

where Q_i^{obs} is the ith measured value, Q_i^{mod} is the ith simulated value, and Q_{mean}^{obs} is the mean value of observed data. The NSE coefficient ranges between -∞ and 1.0, is equal to 1 in case of a perfect agreement, and, generally, values between 0.0 and 1.0 are considered acceptable (Moriasi et al., 2007). The NSE has been used because it is often reported to be the best measure for evaluating the overall fit of a hydrograph (Sevat et al., 1991).

Global Sensitivity Analysis

Most existing environmental models include a high number of parameters. This aspect creates a major problem in their application, as the parameter estimation becomes a high-dimensional and mostly nonlinear problem. To solve this problem, several optimization algorithms were developed (Beven and Binley, 1992; Duan et al., 1992; Poli et al., 2007; Vrugt et al., 2003). Moreover, environmental optimization studies are often affected by the equifinality problem (Beven, 2006) when multiple sets of parameters can produce similar results. This problem is exacerbated when the number of parameters is significant and only limited information about their interactions and their effects on the output is available. However, it is not always necessary to include all model parameters in the optimization process because some of them could be measured or estimated, and some may have negligible effects on the output of the model for a particular application. A sensitivity analysis (SA) can identify the most influential parameters and their interactions and how these parameters affect the output (Saltelli et al., 2005).

The principal steps of a SA are: Factors Prioritization (FP), Factors Fixing (FF), Variance Cutting (VC), and Factors Mapping (FM) (Saltelli and Tarantola, 2004). The aim of FP is to

identify factors that one should measure in order to obtain the greatest reduction in the uncertainty of the output. Conversely, FF identifies factors that are non-influential. By applying these two settings, the modeler is able to reduce the dimension of the optimization problem and have a complete appreciation of the parameters' influences and interactions.

Most SAs performed in the literature of environmental sciences are the so-called 'one-at-a-time' (OAT) sensitivity analyses, performed by changing the value of parameters one-at-a-time while keeping the others constant (Cheviron and Coquet, 2009; Houska et al., 2013; Rezaei et al., 2015). However, when the model includes interactions between parameters, results of the OAT analysis are inaccurate because parameter interactions can be identified only by changing multiple parameters simultaneously. For this reason, when the property of a model is a priori unknown, a Global Sensitivity Analysis (GSA) is always preferred (Saltelli and Annoni, 2010). Practitioners call this analysis a model-free setting.

One of the most widespread algorithms for the GSA is the variance-based Sobol' method (Sobol', 2001). Variance-based methods aim to quantify the amount of variance that each parameter contributes to the unconditional variance of the model output. For the Sobol' method, these amounts are represented by Sobol's sensitivity indices (SI's). These indices give quantitative information about the variance associated with a single parameter or related to interactions of multiple parameters. For a more complete explanation about the Sobol' method, please refer to Sobol' (2001).

Sobol's sensitivity indices are expressed as follows:

$$First\ Order \quad S_i = \frac{V_i}{V} \tag{9}$$

$$Second\ Order \quad S_{ij} = \frac{V_{ij}}{V} \tag{10}$$

$$Total \quad S_T = S_i + \sum_{j \neq i} S_{ij} + \ldots \tag{11}$$

where V_i is the variance associated with the ith parameter and V is the total variance. The first-order index, S_i, is denoted in the literature as the "main effect". This index can be described as the fraction of the model output variance that would disappear when parameter X_i is fixed. When the model is additive, i.e., when it does not include interactions between input factors, then the first-order index is sufficient for decomposing the model's variance. For additive models, the following relation is valid:

$$\sum_i S_i = 1 \tag{12}$$

Even when the model includes interactions between parameters, the first-order index remains the measure to use for FP (Saltelli and Tarantola, 2004). On the other hand, the total effect index, S_T, gives information about a non-additive part of the model. A significant difference between S_T and S_i indicates an important role of an interaction for the parameter considered. Essentially, the total effect index, S_{Ti}, gives a fraction of the total variance that would be left when all factors but X_i were fixed. $S_{Ti} = 0$ is a condition necessary and sufficient for X_i to be non-influential. Therefore, X_i can be fixed at any value within its range of uncertainty without affecting the output unconditional variance. The total effect is the measure to use for FF.

Considering that environmental models are generally highly nonlinear, it is almost impossible to calculate the variances using analytical integrals. Hence, Monte Carlo integrals are often applied, which are based on sampling the parameter space in q samples. Obviously, the accuracy in the estimation of integrals becomes more accurate as the number of samples increases, which also increases the computational cost of the SA. For an accurate description of the calculation of Sobol's indices please refer to Saltelli (2010).

Basically, the calculation of Sobol's indices requires $q \cdot (2p+1)$ model evaluations, where p is the number of input factors. However, Saltelli (2002) introduced a method that requires only $q \cdot (p+2)$ model evaluations. To sample the parameters' space we used Sobol's quasi-random sampling technique (Sobol', 2001).

One of the most important aspects of the GSA is the choice of the number of samples, q. An increase in the number of samples will increase the accuracy of Sobol's indices. However, a high q implies a higher number of model evaluations. The number of samples is case-sensitive; it depends on the structure of the model and on the type of simulations performed. A convergence analysis of Sobol's indices is the recommended procedure for estimating q. However, this approach is time consuming because it needs to repeat the GSA several times by increasing the number of samples until the variability of indices between two consecutive analyses is below a threshold value for all parameters.

In a recent study, Nossent et al. (2011) gave a comprehensive description of the influence of q on the accuracy of a GSA for an environmental model that included 26 parameters. Nossent et al. (2011) reported that for most parameters, less than 5000 samples were sufficient to reach a stable solution. An extensive review of the GSA in hydrological models is reported in Song et al. (2015). Here, we report the number of model runs for each GSA performed, together with the type of GSA, the number of parameters of the model, and the objective function used. For the GSA based on Sobol's method, the number of model runs rarely exceeds 100,000. Due to considerations discussed above, a value of q=5000 was chosen in our study. Table 2 summarizes the characteristics of the GSA for the two scenarios considered.

In order to assess the accuracy of estimations of the sensitivity indices, the bootstrap confidence intervals (BCIs) (Efron and Tibshirani, 1986) were estimated. The basic idea of the bootstrapping is that, in absence of any other information about the distribution, the sample contains all the available information about the underlying distribution. In our particular case, we were interested in computing the uncertainty of estimated sensitivity indices. However, since their distribution is unknown it is not possible to compute the confidence intervals analytically. The rationale of the bootstrap method is to replace the unknown distribution with its empirical distribution and to compute the sensitivity indices using a Monte Carlo simulation approach where samples are generated by resampling the original sample used for the sensitivity analysis. In our

case, the q samples used for the model evaluation were sampled 1000 times with replacement, whereby Sobol's indices were calculated for each resampling. In this way, 95% confidence intervals are constructed by using the percentile method and the moment method (Archer et al., 1997).

The sensitivity analysis was conducted using the programming language Python and in particular, the Sensitivity Analysis Library (SALib) (Usher et al., 2015). An elaborated script overwrites the input file containing the parameters for different materials at each iteration. The script then executes HYDRUS-1D, which usually runs less than one second. If the HYDRUS-1D run is not finished after 15 seconds, it is considered non-convergent; the script then terminates the process and attributes a large negative value to the objective function. The same negative value is attributed when the length of the modeled hydrograph is shorter than one month, which indicates that the run was unsuccessful. Values of the objective function are stored in a one-dimensional array for the subsequent computation of sensitivity indices. Table 3 reports the initial range of all evaluated parameters in the two scenarios. The initial conditions were not included in the GSA because their effects on the hydrograph for a month-long simulation are assumed to be limited to only the first few days.

Monte Carlo Filtering

In the context of an optimization framework, results of the GSA can be used to extract useful information about the problem structure. The GSA preliminarily identifies the subset of input factors that drive most of the variation in the model output; to establish their optimal values, these sensitive parameters can be further investigated by using a Monte Carlo filtering approach. Filtering techniques are used to explore the parameter space pertaining to the single or multiple optima. This is particularly relevant when dealing with mechanistic models that almost always contain ill-defined parameters and are thus referred to as over-parameterized models (Draper and Smith, 1981).

The Monte Carlo filtering is often coupled with the regionalized sensitivity analysis (RSA) (Hornberger and Spear, 1981). The RSA generally requires two tasks: (a) a qualitative description

of the system behavior, and (b) a binary classification of the model output that divides solutions into two behavioral and non-behavioral groups. However, the main drawback of the RSA is that no higher-order analysis is performed and thus interactions between parameters are not investigated. In the GSA, a complete description of main effects and interactions is given. The GSA has been combined effectively with the GLUE analysis (Beven and Binley, 1992) in the context of the parameter optimization (Ratto et al., 2001). In Ratto et al. (2001), the sample generated for the GLUE analysis is also used for the computation of variance-based sensitivity indices.

In this study, the GSA is coupled with a basic Monte Carlo filtering. The aim of this step is to identify *behavioral* regions in the parameter space and to reduce the uncertainty in the following parameter estimation step by using the same sample and runs of the GSA. For each parameter set used in the GSA, a value of the objective function is calculated. Potential solutions are divided into two groups: *behavioral*, solutions with $NSE > 0.0$, and *non-behavioral*, solutions with $NSE \leq 0.0$. Two different types of analysis were performed on the filtered sample: a) Kernel density estimation and b) correlation analysis.

Kernel Density Estimation (KDE)

The KDE plots have been used to identify regions with a high density of *behavioral* solutions. The KDE is a non-parametric estimator of the probability density function (PDF) of a random variable (Silverman, 1981). A kernel is a special type of PDF with an added property that it must be even. The KDE bi-variate plots have been used because they give a smooth qualitative representation of PDFs in a bi-dimensional space. The uni-variate KDE has also been computed for each parameter. The KDE plots have been calculated using a Gaussian kernel and the Scott procedure for the determination of a bandwidth (Scott, 1992).

Correlation Analysis

The correlation analysis helps to identify particular interaction structures between parameters. Detecting high values of correlation coefficients suggests a way to reduce the input factor space. In particular, when the coefficient is positive, the couple of parameters acts in the model as a quotient/difference, and when it is negative, the parameters act as a product/sum.

Particle Swarm Optimization

Inverse modeling is a procedure to estimate unknown parameters of the model from experimental data. One of the major reasons to apply inverse modeling is to estimate parameters that cannot be directly measured for various reasons. Numerous applications of inverse modeling for the estimation of soil hydraulic properties exist in the literature (Abbaspour et al., 2004; Hopmans et al., 2002; Vrugt et al., 2008, 2004). The gradient methods (Marquardt, 1963) have been used most widely among hydrologists and soil scientists. However, these methods are sensitive to the initial values of optimized parameters, and the algorithm often remains trapped in local minima, especially when the response surface exhibits a multimodal behavior. These considerations inspired researchers to develop and use global optimization techniques such as the annealing-simplex method (Pan and Wu, 1998), genetic algorithms (Ines and Droogers, 2002), shuffled complex methods (Vrugt et al., 2003), and ant-colony optimization (Abbaspour et al., 2001), among many others.

In this paper, a global search method based on Particle Swarm Optimization (PSO) (Kennedy and Eberhart, 1995) is used. PSO has been used in multiple studies involving inverse modeling with complex environmental models (Gill et al., 2006; Jiang et al., 2010; Zambrano-Bigiarini and Rojas, 2013). However, so far it has not been used for the determination of unsaturated hydraulic properties. PSO is a relatively new algorithm for evolutionary computation methodology, but its performance has proven to be comparable to various other, more established methodologies (Kennedy and Spears, 1998; Shi and Eberhart, 1999). One of the main advantages of PSO is the easiness of its implementation (Liang et al., 2006). PSO is characterized by an algorithm

based on a social-psychological metaphor involving individuals that interact with each other in a social world. PSO was inspired by the behavior of schools of fish or flocks of birds as they seek food or other resources. In PSO, collections of "particles" explore the search space, looking for a global or near-global optimum. Particles in PSO keep track of their best positions thus far obtained in the search space and the best positions obtained by their neighboring particles. The global best position is what all particles tend to follow. A detailed description of the PSO algorithm is given in Shi and Eberhart (1998).

The most important parameters in the PSO are: c_1, c_2, and w. c_1 and c_2 are constant parameters known as the cognitive and social parameters, respectively, and w is the inertia-weight, which plays a key role in the optimization process by providing balance between exploration and exploitation. A large w facilitates a global search while a small one facilitates a local search. The w parameter is very similar to the "temperature" parameter in the simulated annealing algorithm. While several strategies have been used in the literature for the inertia weight, in this study, a constant value of w has been used (Shi and Eberhart, 1998).

In PSO, each particle is influenced by its σ nearest neighbors. The arrangement of neighbors that influence a particle is called the *topology* of the swarm. Different types of neighborhoods are reported in the literature (Akat and Gazi, 2008). In this study, the *all* topology is used, in which the neighborhood encompasses the entire swarm. The PSO parameters used in this study for both scenarios are reported in Table 4 and are as suggested by Pedersen (2010).

A modified version of the PySwarm Python Library was used for the PSO analysis. Similar to the GSA, a Python script has been written for the optimization process. The script overwrites the input file of HYDRUS-1D containing the hydraulic parameters for the different layers, runs the executable module, and retrieves the value of the objective function. A large negative value of *NSE* is attributed to non-convergent runs, as defined above.

RESULTS AND DISCUSSION

Sensitivity Analysis – Scenario I

As discussed above, the basic outcome of Sobol's SA are the first-order (S_1) and total (S_T) sensitivity indices. Table 5 presents these two indices and their relative bootstrap confidence intervals (BCI). In the left part of Table 5 (S_1), it can be seen that only two parameters exhibit a significant direct influence on the output's variance, the pore-size distribution index n_1 and the air-entry pressure parameter a_1 . The third most influential parameter, the saturated hydraulic conductivity K_{s1}, has the effect, which is only half of the second most influential parameter, a_1. Ten parameters have a first-order index lower than 1%, which indicates that their main effect on the output variance is negligible. Table 5 also shows that the sum of all first-order indices is less than 1, which means that the model is non-additive. Only 56% of variance is attributable to the first-order effects, which indicates that interactions between parameters play a fundamental role.

The right part of Table 5 (S_T) shows that almost 75% of variance in simulated outflow is caused by n_1, either by the variation of the parameter itself (30%) or by interactions with other parameters. Together with a_1 (51%) and K_{s1} (42%), it is the most influential parameter for simulated flow. It can be noted that the saturated hydraulic conductivity, K_{s1}, has a relatively low main effect but a relatively high total effect. That indicates that this parameter has a limited direct effect on the variance of the objective function, but it has an effect in interactions with other parameters.

The effect of the sub-base layer on the output is less significant, while the wear layer strongly conditions the output. That behavior is in agreement with results reported in the literature. Illgen et al. (2007), in his laboratory campaign, confirmed that the wear layer has the major influence on the infiltration capacity of the permeable pavement, while the base and sub-base layers have a minor impact and act as a storage tank. The total index is always greater than zero, which implies that all parameters influence the output variance either directly or by their interactions, and thus no parameter can be fixed without affecting the uncertainty of the output.

Scatter plots for the plain Monte Carlo runs for the two most sensitive parameters, a_1 and n_1, are displayed in Figure 3. The scatter plots show that there is no clear pattern of factors driving bad

567 solutions. Particular trends in the solutions were further identified by the regression lines. They
568 indicate that there is a trend for parameter a_1, with admissible solutions in the left part of the plot.
569 On the other hand, the distribution of values for parameter n_1 is flat, and thus no conclusions can be
570 made about the position of a denser region of *behavioral* solutions in the high-dimensional space.
571
572 ***Monte Carlo Filtering – Scenario I***
573 A Monte Carlo Filtering procedure was applied to the runs of the GSA. The threshold value
574 of $NSE = 0.0$ produced a filtered sample composed of 1,452 *behavioral* solutions. Figure 4 shows
575 the univariate and bivariate KDE plots and the correlation plots for the wear layer.
576 The maximum Pearson correlation coefficient (in absolute values) was 0.42 between
577 parameters a_1 and n_1. It is also evident from Figure 4 that a moderate negative correlation is present
578 for parameters θ_{s1}-a_1, and a positive correlation for parameters θ_{s1}- n_1, while for the other
579 parameters, the correlation is negligible. The univariate KDEs for parameters θ_{s1}, n_1, and K_{s1}
580 indicate a platykurtic distribution of *behavioral* solutions characterized by multimodality. Parameter
581 a_1 exhibits a leptokurtic distribution, for which a denser region of good solutions is clearly
582 identifiable in the range of 0.001-0.1.
583 This behavior is more clear in the bivariate KDE plots. The bivariate KDE for a_1-n_1
584 highlights the presence of a denser region for values of n_1 in the range 2.5-4.5, a behavior that was
585 not evident from the univariate KDE. The comparison between univariate and bivariate plots
586 reveals that the latter gives a much more comprehensive description of the response surface. This
587 aspect is exacerbated when the model is governed by interactions between parameters, which is
588 clearly highlighted by Sobol's indices. In such a case, the high-dimensional inspection of the
589 parameter space provides significant information.
590 The saturated hydraulic conductivity, K_{s1}, for which the univariate KDE indicates a
591 multimodal behavior, exhibits a denser region in the range of 10.0-20.0; this region is clearly
592 identifiable in the bivariate plot of K_1- n_1.

593

594 ***Sensitivity Analysis – Scenario II***

595 Results of the GSA for Scenario II are reported in Table 6. Also for Scenario II, parameters
596 a_1 and n_1 exhibit the highest main effects on the output's variance (about 35%). For Scenario II, the
597 differences are even more evident than for Scenario I. Parameters n_1 and a_1 have a first-order index
598 of 30% and 5%, respectively, while all remaining parameters remain well under 5%. Nine
599 parameters have a first-order index lower than 1%. The main effects represent 53% of the output
600 variance, which clearly indicates both that the model output is again (similarly as for Scenario I)
601 partially driven by interactions between parameters, and that the model is non-additive.

602 The right part of Table 6 (S_T) shows that the output variance is largely influenced by n_1,
603 either directly (30%) or by interactions with other parameters (64%). Similar to Scenario I,
604 parameters a_1 and n_1 are the most influential parameters, and the model's output is mainly driven by
605 the wear layer. Four of the first eight most influential parameters are related to the wear layer. The
606 main difference between Scenarios I and II is the influence of the base and sub-base layers on the
607 model's output. This is evident from Figure 5, in which the average S_T for each layer is reported for
608 both scenarios. For both scenarios, modeling results are most sensitive to the wear layer, which
609 strongly influences the output's variance. However in Scenario II, the influence of the wear layer is
610 partially reduced and redistributed to other layers. It is evident that the adoption of the dual-porosity
611 model for the unsaturated hydraulic properties significantly affects the influence of the base and
612 sub-base layers on the model's output. The dynamics of sensitivity indices between the two
613 scenarios suggest that the physical description of unsaturated flow in the sub-base layer is an
614 important element in numerical simulations.

615 Similar to scenario I, all parameters influence the model's output, either by the variation of
616 the parameters themselves or by their mutual interactions. The condition for FF is never achieved
617 for all parameters.

Scatter plots for the plain Monte Carlo runs for the two most sensitive parameters, $a_1$and n_1, are displayed in Figure 6. It can be seen that there is again no clear pattern of factors driving bad solutions. The regression lines indicate that there is a slight trend, which is higher for parameter a_1, to have admissible solutions in the left part of the plot. The optimum appears flat, however.

Monte Carlo Filtering – Scenario II

A Monte Carlo Filtering procedure was again applied to the runs of the GSA. The filtered sample now consisted of 28,107 *behavioral* solutions. The filtered sample of *behavioral* solutions for Scenario II was considerably larger than for Scenario I. This indicates that the implementation of the dual-porosity model leads to higher values of the objective function.

Figure 7 shows the univariate and bivariate KDE plots as well as the correlation plots for parameters of the wear layer. It is evident that no clear correlation exists between various parameters (Fig. 7), except for a negative correlation trend between parameters a_1 and n_1, but only with a small magnitude. The maximum correlation coefficient, in absolute values, was -0.531 between parameters a_4 and n_4.

The univariate KDE for parameters θ_{s1}-K_{s1} indicates a platykurtic distribution of *behavioral* solutions without a clear identification of a denser region across the parameter space. On the other hand, for parameters a_1 and n_1, the univariate KDEs indicate a more leptokurtic distributions, especially for n_1, for which a denser region of solutions between1.1-2.8 is identifiable.

The bivariate KDEs give a better description of the location of *behavioral* regions in the bidimensional parameter space than the univariate KDEs. The bivariate KDE for the two most sensitive parameters, a_1 and n_1, indicate the presence of a denser region in the range of n_1=(1.1, 2.8), and a_1=(0.01,0.15). The bivariate plots, θ_{s1}- a_1 and θ_{s1}- n_1, indicate the presence of a denser region in the range of θ_{s1}=(0.25, 0.40), a region that was not clearly indicated by the univariate plot for θ_{s1}. The saturated hydraulic conductivity, K_{s1}, exhibits a multimodal behavior characterized by

643 several potential regions of interest. A potential *behavioral* region may be identified in the range of
644 K_{s1}=(7.0, 15.0).
645
646 ***Particle Swarm Optimization***
647 The results and conclusions from the coupled GSA-Monte Carlo filtering analysis were used
648 to reduce the ranges of parameters for the PSO. The reduction was applied only for parameters that
649 exhibited well identifiable *behavioral* regions in multivariate plots. The original ranges were kept
650 for parameters that displayed high multimodality, in order to avoid the convergence of PSO to the
651 local optimum. Table 7 reports the new ranges for all parameters.
652 Figure 8 compares measured and modeled hydrographs for the two scenarios. The PSO for
653 Scenarios I and II resulted in *NSE* values of 0.43 and 0.81, respectively. Both *NSE* values of the
654 objective function are higher than zero and thus admissible (Moriasi et al., 2007). However, the
655 implementation of the dual-porosity model for the base and sub-base layers in Scenario II provides
656 a more accurate description of the hydraulic behavior of the permeable pavement. In particular, the
657 dual-porosity model is able to accurately reproduce the fast hydraulic response of the permeable
658 pavement and the long-tailing behavior of the measured hydrograph. The modeled hydrograph for
659 Scenario I appears less accurate in reproducing the dynamics of the observed hydrograph, especially
660 the fast response of the pavements to precipitation.
661 Optimized parameters for the two scenarios are reported in Table 8. Significant differences
662 emerge between the two scenarios in terms of estimated values of the saturated water contents, θ_{s1}
663 and a_1; differences between estimated values of the saturated hydraulic conductivities, K_{s1} and n_1,
664 are less pronounced. For layer 2, while estimated values of saturated water contents are very
665 similar, huge differences arise between estimated pore-size distribution indices, n_2, which for
666 Scenario I is less than half of its value for Scenario II. Also, K_{s2} is considerably lower for Scenario
667 II than for Scenario I. Estimated vaues of dual-porosity parameters confirm the assumptions made
668 about the fractured nature of the base and subbase layers. While the saturated water content for the

669 mobile domain is very low, the porous matrix possesses a high storage capacity as indicated by the
670 large value of the immobile saturated water content. In particular, the overall porosity of the base
671 layer is about 40% and 30% for the subbase layer. The result for the base layer is slightly higher
672 than the prescriptions of ICPI, which recommends a porosity of 30-35%. The estimated porosity for
673 the subbase layer is 30%, which is lower than the prescribed porosity of about 40%. This difference
674 can be related to the simplifications made in the mobile-immobile dual porosity model for the
675 description of preferential flow and uncertainties related to the effective graduation of the stone
676 material used. However, the significant increase in the accuracy between the single-porosity model
677 and the dual-porosity model suggests that the hydraulic behavior of the base and subbase layers is
678 strongly affected by fast preferential flows in interconnected fractures and the accumulation of
679 water in the rock matrix. This behavior is in agreement with results reported in the literature. For
680 example, Illgen et al. (2007) reported that the water contents in the base and sub-base layers only
681 marginally increased during rainfall events, and that the lower layers act as a storage tank.
682 Both scenarios exhibit low values of porosity for the base and sub-base layers. For scenario
683 II, the total porosity is divided between the mobile and immobile domains. Flow is restricted only to
684 highly conductive and interconnected fractures, which represent a relatively small part of the
685 domain, while the immobile domain provides the storage capacity. While Scenario II assumes
686 overlapping and interacting continua, Scenario I assumes a single continuum approach for all
687 layers. When the optimized value of porosity is very low, such as for the sub-base layer, it is
688 necessary to interpret the optimized values differently than for typical Richards' type flow. In such
689 case, especially for flow in crushed stones, the model tends to approximate a combination of film
690 flow and fingering that likely occur in this layer. This hydraulic behavior is similar to the one
691 reported, for example, by Hodnet and Bell (1990) for unsaturated flow in a medium composed
692 largely of chalk cobbles. In their study, Tokunaga and Wan (1997) analyzed the influence of film
693 flow on unsaturated flow in fractures. High velocities of film flow measured in their study
694 suggested that film flow contributed significantly to preferential flow in fractured rocks. Our model,

based on a macroscopic description of this fast unsaturated flow, shares some similarities with the active fracture model proposed by Liu et al. (1998). This approach divides the pore space into two parts, active and inactive. Flow and transport occurs only within the active pore space, with the inactive part simply bypassed. Liu et al. (1998) further assumed that van Genuchten (1980) relations are approximately valid for the active pore space. In a separate study, Liu et al. (2003) reports values of porosity between 0.01 and 0.03 for the pore space used with the active fracture model.

Confidence Regions

Since parameter estimation involves a variety of possible errors, including measurement errors, model errors, and numerical errors, an uncertainty analysis of the optimized parameters constitutes an important part of parameter estimation. In order to evaluate the uncertainty associated with the estimated parameters, a confidence region around the best solutions optimized with PSO were calculated using HYDRUS-1D. HYDRUS-1D uses the linear approximation method to identify the confidence region around estimated parameters β, resulting in ellipsoid contours centered at β.

Although restrictive and only approximately valid for nonlinear problems, an uncertainty analysis provides a means to compare confidence intervals between parameters, thereby indicating which parameters should be independently measured or estimated. Confidence intervals have been calculated using the Student's *t* distribution with a confidence level of 95%. It is evident from Table 9 that confidence intervals are narrower for Scenario II, and that the most uncertain parameters are the saturated hydraulic conductivities for different layers.

Model Validation

In order to evaluate the reliability of the estimated parameters, the model has been validated on another independent set of experimental data. Figure 10**Error! Bookmark not defined.** shows a

720 comparison between measured and modeled hydrographs for the two scenarios during the validation
721 period.

722 The value of the objective functions are *NSE* = 0.43 for Scenario I and *NSE* = 0.86 for
723 Scenario II. For Scenario I, the value of the objective function remains the same, which confirms
724 the reliability of the calibrated model. Although the simulated hydrograph provides an overall
725 sufficiently accurate description of the hydraulic behavior of the pavement, it is less accurate during
726 rainfall events, which may be a time period of main interest. For Scenario II, the value of the
727 objective function actually increased and reached the value *NSE* = 0.86, which is very high and
728 reflects the accuracy of the modeled hydrograph. Also the description of the hydraulic behavior of
729 the pavement during rainfall events is optimal. This capability of the calibrated model is important
730 when dealing with the analysis of combined traditional drainage systems and LID techniques. A
731 correct description of the hydrograph during precipitation gives information about the lag time and
732 the intensity of peak flow, which are fundamental for both a comprehensive hydraulic analysis of
733 drainage systems, and for the evaluation of benefits of LIDs implementation. The initial part of the
734 hydrograph appears to be underestimated, which may be related to the influence of the unknown
735 initial conditions. The model was not able to reproduce outflow induced by the precipitation event
736 on March 15. This may be related to an overestimation of potential evaporation calculated using a
737 literature value of albedo, which could result in an overestimation of the storage capacity of the
738 pavement at the beginning of the precipitation event, which had a total volume of 6 mm. As a result,
739 the model predicted that the pavement retained all the precipitation volume. A better
740 characterization of evaporation could help in increasing the accuracy of the model, which is already
741 high.

742 Figure 10 directly compares the measured outflows with those calculated by the two
743 modeling scenarios. The red bisector line represents conditions when modeled and measured
744 outflows are perfectly matched. Linear regression lines are reported for both scenarios. Since the
745 Scenario I tends to overestimate the outflow fluxes, the difference between the bisector and the

linear regression line (gray) for scenario I is substantial. On the other hand, Scenario II tends to only slightly underestimate the outflow fluxes, and thus the slopes of the bisector and the linear regression line (black) for Scenario II are similar. The simulated hydrographs for both scenarios tend to introduce some bias in the estimation of peak flows. This aspect is related to the choice of the *NSE* as the objective function for the optimization. The *NSE* is focused on the general behavior of the hydrograph rather than on particular components such as peak flows. A multi-objective optimization that would include an objective function targeted to peak flow estimates could represent a more appropriate approach if estimates of peak flows were the main goal of calibration. However, even of great interest, the multi-objective optimization is out of the scope of this paper. Overall, the validation process demonstrated the reliability of the calibrated models for both scenarios.

CONCLUSIONS

In this paper, we investigated the suitability of the mechanistic model, HYDRUS-1D, to correctly describe the hydraulic behavior of a permeable pavement installed at the University of Calabria. We considered two different scenarios in describing the system. In Scenario I, we assumed that flow on all layers can be described using a single-porosity model, while in Scenario II, we assumed that a dual-porosity mobile-immobile model is needed to describe flow in the base and subbase layers. The widely used Nash-Sutcliffe efficiency index was used to assess the models. A Global Sensitivity Analysis, coupled with a Monte Carlo filtering procedure, was carried out before the model calibration. Sensitivity analysis results suggested that the model is non-additive and mainly driven by parameter interactions in both scenarios. The first-order effects only accounted for 56% of output variance for Scenario I and 53% for Scenario II. Sensitivity analysis also revealed that the wear layer mainly influenced the hydraulic behavior of the pavement. A subsequent Monte Carlo filtering procedure was applied to the runs performed during the sensitivity analysis in order to identify the *behavioral* regions and to reduce parameter uncertainty. Both univariate and bivariate

Kernel Density Estimation plots were used to inspect the response surfaces and identify the *behavioral* regions. This analysis revealed the high multimodality of the response surfaces, which suggested the use of a global optimization algorithm for parameter estimation. Correlation coefficients of the filtered sample were also computed, indicating a general low correlation between parameters. Based on the results of the Monte Carlo filtering, a heuristic global optimization method based on the Particle Swarm algorithm was used for parameter estimation. The calibrated model for Scenario I exhibited an optimum $NSE = 0.43$, while for Scenario II, it reached $NSE=0.81$. The optimized parameters were then validated against an independent set of experimental data, resulting in $NSE = 0.43$ for Scenario I and $NSE = 0.86$ for Scenario II. The results of optimization and validation clearly indicated that the implementation of the dual-porosity model for the base and subbase layers produced more accurate results than the single-porosity model and described much better the hydraulic behavior of pervious pavement. Results also confirmed the validity of the assumption that the hydraulic behavior of the base and subbase layers was similar to the behavior of a fractured rock, which is characterized by the highly permeable interconnected fractures and the highly storative rock matrix. The main advantage in using a simple, dual-porosity, mobile-immobile model with a saturation-based mass transfer is that this model requires only two additional parameters compared to the single-porosity model. Further significant improvements could be obtained by characterizing the hydraulic properties of the wear layer in the laboratory, as suggested by the sensitivity analysis.

Acknowledgements

The study was co-funded by the Italian National Operative Project (PON)—Research and Competitiveness for the convergence regions 2007/2013-I Axis “Support to structural changes” operative objective 4.1.1.1. “Scientific-technological generators of transformation processes of the productive system and creation of new sectors” Action II: “Interventions to support industrial research”.

REFERENCES

Abbaspour, K.C., Johnson, C.A., van Genuchten, M.T., 2004. Estimating Uncertain Flow and Transport Parameters Using a Sequential Uncertainty Fitting Procedure. Vadose Zo. J. 3, 1340–1352. doi:10.2113/3.4.1340

Abbaspour, K.C., Schulin, R., van Genuchten, M.T., 2001. Estimating unsaturated soil hydraulic parameters using ant colony optimization. Adv. Water Resour. 24, 827–841. doi:10.1016/S0309-1708(01)00018-5

Akat, S.B., Gazi, V., 2008. Particle swarm optimization with dynamic neighborhood topology: Three neighborhood strategies and preliminary results, in: 2008 IEEE Swarm Intelligence Symposium. pp. 1–8. doi:10.1109/SIS.2008.4668298

Allen, R.G., Pereira, L.S., Raes, D., Smith, M., 1998. FAO Irrigation and Drainage Paper No. 56: Crop Evapotranspiration, FAO. Rome.

Archer, G.E.B., Saltelli, A., Sobol, I.M., 1997. Sensitivity measures,anova-like Techniques and the use of bootstrap. J. Stat. Comput. Simul. 58, 99–120. doi:10.1080/00949659708811825

Bai, M., Ma, Q., Roegiers, J.-C., 1994. A nonlinear dual-porosity model. Appl. Math. Model. 18, 602–610. doi:10.1016/0307-904X(94)90318-2

Barenblatt, G.., Zheltov, I.., Kochina, I.., 1960. Basic concepts in the theory of seepage of homogeneous liquids in fissured rocks [strata]. J. Appl. Math. Mech. 24, 1286–1303. doi:10.1016/0021-8928(60)90107-6

Bengtsson, L., Grahn, L., Olsson, J., 2004. Hydrological function of a thin extensive green roof in southern Sweden. Nord. Hydrol. 36, 259–268.

Berardi, U., GhaffarianHoseini, A., GhaffarianHoseini, A., 2014. State-of-the-art analysis of the environmental benefits of green roofs. Appl. Energy 115, 411–428. doi:10.1016/j.apenergy.2013.10.047

Beven, K., 2006. A manifesto for the equifinality thesis. J. Hydrol. 320, 18–36. doi:10.1016/j.jhydrol.2005.07.007

Beven, K., Binley, A., 1992. The future of distributed models: Model calibration and uncertainty prediction. Hydrol. Process. 6, 279–298. doi:10.1002/hyp.3360060305

Brattebo, B.O., Booth, D.B., 2003. Long-term stormwater quantity and quality performance of permeable pavement systems. Water Res. 37, 4369–76. doi:10.1016/S0043-1354(03)00410-X

Carbone, M., Brunetti, G., Piro, P., 2014. Hydrological Performance of a Permeable Pavement in Mediterranean Climate, in: 14th SGEM GeoConference on Water Resources. Forest, Marine And Ocean Ecosystems. pp. 381–388. doi:10.5593/SGEM2014/B31/S12.050

Carbone, M., Brunetti, G., Piro, P., 2015a. Modelling the Hydraulic Behaviour of Growing Media with the Explicit Finite Volume Solution. Water 7, 568–591. doi:10.3390/w7020568

Carbone, M., Turco, M., Brunetti, G., Piro, P., 2015b. A Cumulative Rainfall Function for Subhourly Design Storm in Mediterranean Urban Areas. Adv. Meteorol. 2015, 1–10. doi:10.1155/2015/528564

Cheviron, B., Coquet, Y., 2009. Sensitivity Analysis of Transient-MIM HYDRUS-1D: Case Study Related to Pesticide Fate in Soils. Vadose Zo. J. 8, 1064. doi:10.2136/vzj2009.0023

Coffman, L.S., 2002. Low-impact development: an alternative stormwater management technology., in: France, R.L. (Ed.), Handbook of Water Sensitive Planning and Design. Lewis Publishers Inc., pp. 97–123.

Collins, K.A., Hunt, W.F., Hathaway, J.M., 2008. Hydrologic Comparison of Four Types of Permeable Pavement and Standard Asphalt in Eastern North Carolina. J. Hydrol. Eng. 13, 1146–1157. doi:10.1061/(ASCE)1084-0699(2008)13:12(1146)

Davis, A.P., 2008. Field Performance of Bioretention: Hydrology Impacts. J. Hydrol. Eng. 13, 90–95. doi:10.1061/(ASCE)1084-0699(2008)13:2(90)

845 DeWalle, D.R., Swistock, B.R., Johnson, T.E., McGuire, K.J., 2000. Potential effects of climate
846 change and urbanization on mean annual streamflow in the United States. Water Resour. Res.
847 36, 2655–2664. doi:10.1029/2000WR900134
848 Draper, N., Smith, H., 1981. Applied regression analysis 2nd ed., Technometrics.
849 doi:10.1198/tech.2005.s303
850 Duan, Q., Sorooshian, S., Gupta, V., 1992. Effective and efficient global optimization for
851 conceptual rainfall-runoff models. Water Resour. Res. 28, 1015–1031.
852 doi:10.1029/91WR02985
853 Efron, B., Tibshirani, R., 1986. Bootstrap Methods for Standard Errors, Confidence Intervals, and
854 Other Measures of Statistical Accuracy. Stat. Sci. 1, 54–75.
855 Elliot, A., Trowsdale, S., 2007. A review of models for low impact urban stormwater drainage.
856 Environ. Model. Softw. 22, 394–405. doi:10.1016/j.envsoft.2005.12.005
857 Fassman, E. a., Blackbourn, S., 2010. Urban Runoff Mitigation by a Permeable Pavement System
858 over Impermeable Soils. J. Hydrol. Eng. 15, 475–485. doi:10.1061/(ASCE)HE.1943-
859 5584.0000238
860 Geiger, S., Cortis, A., Birkholzer, J.T., 2010. Upscaling solute transport in naturally fractured
861 porous media with the continuous time random walk method. Water Resour. Res. 46, n/a–n/a.
862 doi:10.1029/2010WR009133
863 Gill, M.K., Kaheil, Y.H., Khalil, A., McKee, M., Bastidas, L., 2006. Multiobjective particle swarm
864 optimization for parameter estimation in hydrology. Water Resour. Res. 42, n/a–n/a.
865 doi:10.1029/2005WR004528
866 Gironás, J., Roesner, L. a, Rossman, L. a, Davis, J., 2010. A new applications manual for the Storm
867 Water Management Model (SWMM). Environ. Model. Softw. 25, 813–814.
868 doi:10.1016/j.envsoft.2009.11.009
869 Hilten, R.N., Lawrence, T.M., Tollner, E.W., 2008. Modeling stormwater runoff from green roofs
870 with HYDRUS-1D. J. Hydrol. 358, 288–293. doi:10.1016/j.jhydrol.2008.06.010
871 Hodnet, M.G., Bell, J.P., 1990. Processes of water movement through a chalk coombe deposit in
872 Southeast England. Hydrol. Process. 4, 361–372. doi:10.1002/hyp.3360040406
873 Hopmans, J.W., Šimůnek, J., Romano, N., Durner, W., 2002. Inverse Modeling of Transient Water
874 Flow, in: Dane, J.H., Topp, G.C. (Eds.), Methods of Soil Analysis, Part 4, Physical Methods.
875 SSSA, Madison, WI, pp. 963–1008.
876 Hornberger, G.M., Spear, R.C., 1981. An approach to the preliminary analysis of environmental
877 systems. J. Environ. Manage. 12, 7–12. doi:10.1016/S0272-4944(89)80026-X
878 Houska, T., Multsch, S., Kraft, P., Frede, H.-G., Breuer, L., 2013. Monte Carlo based calibration
879 and uncertainty analysis of a coupled plant growth and hydrological model. Biogeosciences
880 Discuss. 10, 19509–19540. doi:10.5194/bgd-10-19509-2013
881 Illgen, M., Harting, K., Schmitt, T.G., Welker, A., 2007. Runoff and infiltration characteristics of
882 pavement structures--review of an extensive monitoring program. Water Sci. Technol. 56,
883 133–40. doi:10.2166/wst.2007.750
884 Ines, A.V.M., Droogers, P., 2002. Inverse modelling in estimating soil hydraulic functions: a
885 Genetic Algorithm approach. Hydrol. Earth Syst. Sci. Discuss. 6, 49–66.
886 Jiang, Y., Liu, C., Huang, C., Wu, X., 2010. Improved particle swarm algorithm for hydrological
887 parameter optimization. Appl. Math. Comput. 217, 3207–3215.
888 doi:10.1016/j.amc.2010.08.053
889 Kennedy, J., Eberhart, R., 1995. Particle Swarm Optimization. Eng. Technol. 1942–1948.
890 Kennedy, J., Spears, W.M., 1998. Matching algorithms to problems: an experimental test of the
891 particle swarm and some genetic algorithms on the multimodal problem generator, in: 1998
892 IEEE International Conference on Evolutionary Computation Proceedings. IEEE World
893 Congress on Computational Intelligence (Cat. No.98TH8360). IEEE, pp. 78–83.
894 doi:10.1109/ICEC.1998.699326

Kundzewicz, Z., Radziejewski, M., Pínskwar, I., 2006. Precipitation extremes in the changing climate of Europe. Clim. Res. 31, 51–58. doi:10.3354/cr031051

Levinson, R., Akbari, H., 2002. Effects of composition and exposure on the solar reflectance of portland cement concrete. Cem. Concr. Res. 32, 1679–1698. doi:10.1016/S0008-8846(02)00835-9

Li, Y., Babcock, R.W., 2015. Modeling Hydrologic Performance of a Green Roof System with HYDRUS-2D. J. Environ. Eng. 141, 04015036. doi:10.1061/(ASCE)EE.1943-7870.0000976

Liang, J.J., Qin, A.K., Suganthan, P.N., Baskar, S., 2006. Comprehensive learning particle swarm optimizer for global optimization of multimodal functions. IEEE Trans. Evol. Comput. 10, 281–295. doi:10.1109/TEVC.2005.857610

Liu, H.H., Doughty, C., Bodvarsson, G.S., 1998. An active fracture model for unsaturated flow and transport in fractured rocks. Water Resour. Res. 34, 2633–2646. doi:10.1029/98WR02040

Liu, H.-H., Haukwa, C.B., Ahlers, C.F., Bodvarsson, G.S., Flint, A.L., Guertal, W.B., 2003. Modeling flow and transport in unsaturated fractured rock: an evaluation of the continuum approach. J. Contam. Hydrol. 62-63, 173–188. doi:10.1016/S0169-7722(02)00170-5

Marquardt, D.W., 1963. An Algorithm for Least-Squares Estimation of Nonlinear Parameters. J. Soc. Ind. Appl. Math. 11, 431–441. doi:10.1137/0111030

Min, S.-K., Zhang, X., Zwiers, F.W., Hegerl, G.C., 2011. Human contribution to more-intense precipitation extremes. Nature 470, 378–81. doi:10.1038/nature09763

Moriasi, D.N., Arnold, J.G., Van Liew, M.W., Binger, R.L., Harmel, R.D., Veith, T.L., 2007. Model evaluation guidelines for systematic quantification of accuracy in watershed simulations. Trans. ASABE 50, 885–900. doi:10.13031/2013.23153

Nash, J.E., Sutcliffe, J. V, 1970. River Flow Forecasting through Conceptual Models: Part I - A Discussion of Principles. J. Hydrol. 10, 282–290. doi:10.1016/0022-1694(70)90255-6

Newcomer, M.E., Gurdak, J.J., Sklar, L.S., Nanus, L., 2014. Urban recharge beneath low impact development and effects of climate variability and change. Water Resour. Res. 50, 1716–1734. doi:10.1002/2013WR014282

Palla, A., Gnecco, I., Lanza, L.G., 2009. Unsaturated 2D modelling of subsurface water flow in the coarse-grained porous matrix of a green roof. J. Hydrol. doi:10.1016/j.jhydrol.2009.10.008

Pan, L., Wu, L., 1998. A hybrid global optimization method for inverse estimation of hydraulic parameters: Annealing-simplex method. Water Resour. Res. 34, 2261–2269. doi:10.1029/98WR01672

Pedersen, M.E.H., 2010. Good parameters for particle swarm optimization, Technical Report HL1001, Hvass Laboratories.

Poli, R., Kennedy, J., Blackwell, T., 2007. Particle swarm optimization. Swarm Intell. 1, 33–57. doi:10.1007/s11721-007-0002-0

Price, K., 2011. Effects of watershed topography, soils, land use, and climate on baseflow hydrology in humid regions: A review. Prog. Phys. Geogr. 35, 465–492. doi:10.1177/0309133311402714

Ratto, M., Tarantola, S., Saltelli, A., 2001. Sensitivity analysis in model calibration: GSA-GLUE approach. Comput. Phys. Commun. 136, 212–224. doi:10.1016/S0010-4655(01)00159-X

Rezaei, M., Seuntjens, P., Joris, I., Boënne, W., Van Hoey, S., Campling, P., Cornelis, W.M., 2015. Sensitivity of water stress in a two-layered sandy grassland soil to variations in groundwater depth and soil hydraulic parameters. Hydrol. Earth Syst. Sci. Discuss. 12, 6881–6920. doi:10.5194/hessd-12-6881-2015

Rose, S., Peters, N.E., 2001. Effects of urbanization on streamflow in the Atlanta area (Georgia, USA): a comparative hydrological approach. Hydrol. Process. 15, 1441–1457. doi:10.1002/hyp.218

Saltelli, A., 2002. Making best use of model evaluations to compute sensitivity indices. Comput. Phys. Commun. 145, 280–297. doi:10.1016/S0010-4655(02)00280-1

945 Saltelli, A., Annoni, P., 2010. How to avoid a perfunctory sensitivity analysis. Environ. Model.
946 Softw. 25, 1508–1517. doi:10.1016/j.envsoft.2010.04.012
947 Saltelli, A., Annoni, P., Azzini, I., Campolongo, F., Ratto, M., Tarantola, S., 2010. Variance based
948 sensitivity analysis of model output. Design and estimator for the total sensitivity index.
949 Comput. Phys. Commun. 181, 259–270. doi:10.1016/j.cpc.2009.09.018
950 Saltelli, A., Tarantola, S., 2004. Sensitivity Analysis in Practice: A Guide to Assessing Scientific
951 Models 232.
952 Saltelli, A., Tarantola, S., Saisana, M., Nardo, M., 2005. What is sensitivity analysis?, in: II
953 Convegno Della Rete Dei Nuclei Di Valutazione E Verifica, Napoli 26, 27 Gennaio 2005,
954 Centro Congressi Universitá Federico II, Via Partenope 36.
955 Scott, D.W., 1992. Frontmatter, Wiley Series in Probability and Mathematical Statistics Applied
956 Probability and Statistics Section. doi:10.1002/9780470316849.fmatter
957 Sevat, E., Dezetter, A., Servat, E., 1991. Selection of calibration objective functions in the context
958 of rainfall-runoff modelling in a sudanese savannah area. Hydrol. Sci. - J. - des Sci. Hydrol.
959 36, 307–330. doi:10.1080/02626669109492517
960 Shi, Y., Eberhart, R., 1998. A modified particle swarm optimizer. 1998 IEEE Int. Conf. Evol.
961 Comput. Proceedings. IEEE World Congr. Comput. Intell. (Cat. No.98TH8360) 69–73.
962 doi:10.1109/ICEC.1998.699146
963 Shi, Y., Eberhart, R.C., 1999. Empirical study of particle swarm optimization. Proc. 1999 Congr.
964 Evol. Comput. 1945–1950. doi:10.1109/CEC.1999.785511
965 Silverman, B., 1981. Using kernel density estimates to investigate multimodality. J. R. Stat. Soc.
966 43, 97–99.
967 Simmons, D.L., Reynolds, R.J., 1982. EFFECTS OF URBANIZATION ON BASE FLOW OF
968 SELECTED SOUTH-SHORE STREAMS, LONG ISLAND, NEW YORK. J. Am. Water
969 Resour. Assoc. 18, 797–805. doi:10.1111/j.1752-1688.1982.tb00075.x
970 Simunek, J., Jarvis, N.J., van Genuchten, M.T., Gardenas, A., 2003. Review and comparison of
971 models for describing non-equilibrium and preferential flow and transport in the vadose zone.
972 J. Hydrol. 272, 14–35. doi:10.1016/S0022-1694(02)00252-4
973 Šimůnek, J., van Genuchten, M.T., 2008. Modeling Nonequilibrium Flow and Transport Processes
974 Using HYDRUS. Vadose Zo. J. 7, 782. doi:10.2136/vzj2007.0074
975 Šimůnek, J., van Genuchten, M.T., Šejna, M., 2008. Development and Applications of the
976 HYDRUS and STANMOD Software Packages and Related Codes. Vadose Zo. J. 7, 587.
977 doi:10.2136/vzj2007.0077
978 Sobol′, I.., 2001. Global sensitivity indices for nonlinear mathematical models and their Monte
979 Carlo estimates. Math. Comput. Simul. 55, 271–280. doi:10.1016/S0378-4754(00)00270-6
980 Song, X., Zhang, J., Zhan, C., Xuan, Y., Ye, M., Xu, C., 2015. Global sensitivity analysis in
981 hydrological modeling: Review of concepts, methods, theoretical framework, and applications.
982 J. Hydrol. 523, 739–757. doi:10.1016/j.jhydrol.2015.02.013
983 Tokunaga, T.K., Wan, J., 1997. Water film flow along fracture surfaces of porous rock. Water
984 Resour. Res. 33, 1287–1295. doi:10.1029/97WR00473
985 Trimble, S.W., 1997. Contribution of Stream Channel Erosion to Sediment Yield from an
986 Urbanizing Watershed. Science (80-.). 278, 1442–1444. doi:10.1126/science.278.5342.1442
987 Usher, W., xantares, Hadka, D., bernardoct, Fernando, Herman, J., Mutel, C., 2015. SALib: New
988 documentation, doc strings and installation requirements. doi:10.5281/zenodo.31316
989 Van Genuchten, M.T., 1980. A Closed-form Equation for Predicting the Hydraulic Conductivity of
990 Unsaturated Soils1. Soil Sci. Soc. Am. J. 44, 892–898.
991 doi:10.2136/sssaj1980.03615995004400050002x
992 Van Genuchten, M.T., Wierenga, P.J., 1976. Mass Transfer Studies in Sorbing Porous Media I.
993 Analytical Solutions. Soil Sci. Soc. Am. J. 40, 473–480.

994 Vrugt, J.A., Gupta, H. V., Bouten, W., Sorooshian, S., 2003. A Shuffled Complex Evolution
995 Metropolis algorithm for optimization and uncertainty assessment of hydrologic model
996 parameters. Water Resour. Res. 39, n/a–n/a. doi:10.1029/2002WR001642
997 Vrugt, J.A., Schoups, G., Hopmans, J.W., Young, C., Wallender, W.W., Harter, T., Bouten, W.,
998 2004. Inverse modeling of large-scale spatially distributed vadose zone properties using global
999 optimization. Water Resour. Res. 40, n/a–n/a. doi:10.1029/2003WR002706
1000 Vrugt, J.A., Stauffer, P.H., Wöhling, T., Robinson, B.A., Vesselinov, V. V., 2008. Inverse
1001 Modeling of Subsurface Flow and Transport Properties: A Review with New Developments.
1002 Vadose Zo. J. 7, 843. doi:10.2136/vzj2007.0078
1003 Warren, J.E., Root, P.J., 1963. The Behavior of Naturally Fractured Reservoirs. Soc. Pet. Eng. J. 3,
1004 245–255. doi:10.2118/426-PA
1005 Wasko, C., Sharma, A., 2015. Steeper temporal distribution of rain intensity at higher temperatures
1006 within Australian storms. Nat. Geosci. 8, 527–529. doi:10.1038/ngeo2456
1007 Westra, S., Fowler, H.J., Evans, J.P., Alexander, L. V., Berg, P., Johnson, F., Kendon, E.J.,
1008 Lenderink, G., Roberts, N.M., 2014. Future changes to the intensity and frequency of short-
1009 duration extreme rainfall. Rev. Geophys. 52, 522–555. doi:10.1002/2014RG000464
1010 Whipple, W., DiLouie, J.M., Pytlar, T., 1981. EROSIONAL POTENTIAL OF STREAMS IN
1011 URBANIZING AREAS. J. Am. Water Resour. Assoc. 17, 36–45. doi:10.1111/j.1752-
1012 1688.1981.tb02586.x
1013 Zambrano-Bigiarini, M., Rojas, R., 2013. A model-independent Particle Swarm Optimisation
1014 software for model calibration. Environ. Model. Softw. 43, 5–25.
1015 doi:10.1016/j.envsoft.2013.01.004
1016 Zhang, S., Guo, Y., 2015. SWMM Simulation of the Storm Water Volume Control Performance of
1017 Permeable Pavement Systems. J. Hydrol. Eng. 20, 06014010. doi:10.1061/(ASCE)HE.1943-
1018 5584.0001092

1019

1020

1021 Figure 1. A schematic of the permeable pavement.

1022 Figure 2. Precipitation and subsurface flow during the optimization (top) and validation
1023 (bottom) time periods.

1024 Figure 3. Scatter plots for pair relations a_1-*NSE* (left) and n_1-*NSE* (right) for Scenario I. The
1025 red line is a regression line.

1026 Figure 4. Bivariate KDE plots (below diagonal), univariate KDE plots (diagonal), and
1027 correlation plots (above diagonal) for Scenario I.

1028 Figure 5. The average total index, S_T, for different layers for both scenarios.

1029 Figure 6. Scatter plots for pair relations a_1-*NSE* (left) and n_1-*NSE* (right) for Scenario II. The
1030 red line is a regression line.

1031 Figure 7. Bivariate KDE plots (below diagonal), univariate KDE plots (diagonal), and
1032 correlation plots (above diagonal) for Scenario II.

1033 Figure 8. Comparison between the modeled and measured hydrographs for Scenarios I (top)
1034 and II (bottom) for the optimization process.

1035 Figure 9. Comparison between the modeled and measured hydrograph for the two scenarios
1036 for the validation period.

1037 Figure 10. Comparison between the modeled and measured outflows for the two scenarios
1038 for the validation period.

1039

Soil Layer	Scenario I	Scenario II
Wear	Single Porosity	Single Porosity
Bedding	Single Porosity	Single Porosity
Base	Single Porosity	Dual Porosity – MIM
Sub-base	Single Porosity	Dual Porosity – MIM
Protection	Single Porosity	Single Porosity

1040 Table 1. Conceptual models representing water flow in the permeable pavement.

1041

Scenario	Number of parameters	Model runs
I	16	90000
II	20	110000

1042 Table 2. Number of parameters and HYDRUS-1D runs for both scenarios.

1043

	Scenario I	Scenario II
Parameter	Initial range	
θ_{s1} [-]	0.2-0.5	0.2-0.5
a_1 [1/cm]	0.001-0.3	0.001-0.3
n_1 [-]	1.1-4.5	1.1-4.5
K_{s1} [cm/min]	1.0-20.0	1.0-20.0
θ_{s2} [-]	0.2-0.5	0.2-0.5
a_2 [1/cm]	0.001-0.3	0.001-0.3
n_2 [-]	1.1-4.5	1.1-4.5
K_{s2} [cm/min]	1.0-20.0	1.0-20.0
θ_{s3} [-]	0.01-0.40	0.001-0.1
a_3 [1/cm]	0.001-0.3	0.001-0.3
n_3 [-]	1.1-4.5	1.1-4.5
K_{s3} [cm/min]	1.0-100.0	1.0-100.0
$\theta_{s,im3}$ [-]	-	0.15-0.4
ω_3 [1/min]	-	0.00001-0.009
θ_{s4} [-]	0.01-0.4	0.001-0.1
a_4 [1/cm]	0.001-0.3	0.001-0.3
n_4 [-]	1.1-4.5	1.1-4.5
K_{s4} [cm/min]	1.0-100.0	1.0-100.0
$\theta_{s,im4}$ [-]	-	0.15-0.4
ω_4 [1/min]	-	0.00001-0.009

1044 Table 3. Ranges of parameters used in the GSA for both scenarios.

1045

N	c_1	c_2	w
69	-0.267	3.395	-0.444

1046 Table 4. Parameters used in the PSO optimization.

1047

Parameter	S_1	S_1 (BCI)	Parameter	S_T	S_T (BCI)

n_1 [-]	0.298	0.054	n_1 [-]	0.745	0.042
a_1 [1/cm]	0.102	0.040	a_1 [1/cm]	0.508	0.032
K_{s1} [cm/min]	0.051	0.040	K_{s1} [cm/min]	0.421	0.032
θ_{s3} [-]	0.023	0.024	θ_{s1} [-]	0.247	0.025
a_4 [1/cm]	0.020	0.023	n_4 [-]	0.224	0.146
a_2 [1/cm]	0.017	0.022	K_{s3} [cm/min]	0.210	0.127
n_3 [-]	0.014	0.029	n_3 [-]	0.194	0.035
K_{s4} [cm/min]	0.009	0.025	a_3 [1/cm]	0.181	0.024
n_4 [-]	0.009	0.035	a_2 [1/cm]	0.176	0.024
θ_{s1} [-]	0.009	0.028	n_2 [-]	0.176	0.028
n_2 [-]	0.007	0.023	a_4 [1/cm]	0.170	0.033
K_{s3} [cm/min]	0.004	0.022	θ_{s3} [-]	0.167	0.031
θ_{s4} [-]	0.001	0.022	θ_{s2} [-]	0.151	0.030
a_3 [1/cm]	-0.001	0.024	K_{s2} [cm/min]	0.138	0.023
θ_{s2} [-]	-0.004	0.019	K_{s4} [cm/min]	0.138	0.038
K_{s2} [cm/min]	-0.005	0.016	θ_{s4} [-]	0.136	0.022
Sum	0.563			> 1.0	

Table 5. First-order (S_1) and total (S_T) effect indices (in decreasing order) with their bootstrap confidence intervals (BCI) for parameters of Scenario I.

Parameter	S_1	S_1 **(BCI)**	**Parameter**	S_T	S_T **(BCI)**
n_1 [-]	0.302	0.026	n_1 [-]	0.640	0.023
a_1 [1/cm]	0.054	0.029	a_1 [1/cm]	0.387	0.027
θ_{s3} [-]	0.030	0.045	n_3 [-]	0.383	0.020
n_3 [-]	0.026	0.024	θ_{s3} [-]	0.294	0.027
K_{s3} [cm/min]	0.018	0.022	a_3 [1/cm]	0.291	0.022
a_4 [1/cm]	0.018	0.020	θ_{s1} [-]	0.271	0.019
θ_{s2} [-]	0.017	0.018	a_4 [1/cm]	0.269	0.019
θ_{s4} [-]	0.014	0.022	K_{s1} [cm/min]	0.259	0.018
a_3 [1/cm]	0.013	0.025	n_4 [-]	0.256	0.013
K_{s2} [cm/min]	0.012	0.026	a_2 [1/cm]	0.229	0.017
K_{s4} [cm/min]	0.011	0.031	K_{s3} [cm/min]	0.222	0.017
θ_{s1} [-]	0.007	0.023	n_2 [-]	0.217	0.022
$\theta_{s,im3}$ [-]	0.006	0.017	θ_{s4} [-]	0.201	0.017
a_2 [1/cm]	0.005	0.016	K_{s2} [cm/min]	0.195	0.023
K_{s1} [cm/min]	0.001	0.022	K_{s4} [cm/min]	0.186	0.021
ω_4 [1/min]	-0.001	0.027	θ_{s2} [-]	0.185	0.018
n_2 [-]	-0.001	0.026	$\theta_{s,im3}$ [-]	0.149	0.016
ω_3 [1/min]	-0.003	0.021	ω_3 [1/min]	0.143	0.016
$\theta_{s,im4}$ [-]	-0.004	0.020	$\theta_{s,im4}$ [-]	0.138	0.013
n_4 [-]	-0.006	0.017	ω_4 [1/min]	0.125	0.020
Sum	0.534			> 1.0	

Table 6. First-order (S_1) and total (S_T) effect indices (in decreasing order) with their bootstrap confidence intervals (BCI) for parameter of Scenario II.

	Scenario I	Scenario II
Parameter	Reduced range	
θ_{s1} [-]	0.2-0.5	0.2-0.4
a_1 [1/cm]	0.001-0.1	0.001-0.15
n_1 [-]	3.0-4.5	1.1-2.8
K_{s1} [cm/min]	10.0-20.0	1.5-20.0
θ_{s2} [-]	0.25-0.5	0.2-0.4
a_2 [1/cm]	0.2-0.3	0.1-0.2
n_2 [-]	1.1-4.5	1.1-4.5
K_{s2} [cm/min]	1.0-20.0	3.0-20.0
θ_{s3} [-]	0.20-0.40	0.001-0.05
a_3 [1/cm]	0.001-0.05	0.001-0.05
n_3 [-]	1.1-4.5	1.5-4.5
K_{s3} [cm/min]	1.0-100.0	20.-100.0
$\theta_{s,im3}$ [-]	-	0.2-0.4
ω_3 [1/min]	-	0.00001-0.009
θ_{s4} [-]	0.01-0.2	0.001-0.05
a_4 [1/cm]	0.15-0.3	0.15-0.3
n_4 [-]	2.0-4.0	1.5-3.5
K_{s4} [cm/min]	1.0-100.0	1.0-100.0
$\theta_{s,im4}$ [-]	-	0.15-0.3
ω_4 [1/min]	-	0.00001-0.009

1055 Table 7. Reduced ranges of optimized parameters for the optimization process.

1056

	Scenario I								
Layer	θ_r	θ_s	a	N	K_s	L	$\theta_{r,\mathrm{im}}$	$\theta_{s,\mathrm{im}}$	ω
Wear	0.045	0.2	0.002	3.0	10	0.5	-	-	-
Bedding	0.03	0.3	0.3	4.47	20	0.5	-	-	-
Base	0	0.2	0.023	2.85	68.7	0.5	-	-	-
Sub-base	0	0.01	0.27	2.41	96.7	0.5	-	-	-
Protection	0.03	0.3	0.3	4.47	20	0.5	-	-	-
	Scenario II								
Wear	0.045	0.287	0.03	2.67	7.33	0.5	-	-	-
Bedding	0.03	0.298	0.113	3.04	3.87	0.5	-	-	-
Base	0	0.044	0.021	4.33	93.2	0.5	0	0.35	0.00017
Sub-base	0	0.001	0.247	2.17	56.3	0.5	0	0.29	0.0013
Protection	0.03	0.298	0.113	3.04	3.87	0.5	-	-	-

1057 Table 8. Optimized soil hydraulic parameters for both scenarios.

1058

	Scenario I		Scenario II	
Parameter	**Value**	**CI**	**Value**	**CI**
θ_{s1} [-]	0.2	0.057	0.287	0.007
a_1 [1/cm]	0.002	0.0006	0.029	0.0008
n_1 [-]	3	0.783	2.67	0.058
K_{s1} [cm/min]	10	4.4	7.33	0.272
θ_{s2} [-]	0.3	0.072	0.29	0.009

a_2 [1/cm]	0.3	0.062	0.11	0.002
n_2 [-]	4.47	1.08	3.04	0.052
K_{s2} [cm/min]	20	6.5	3.87	0.084
θ_{s3} [-]	0.2	0.048	0.044	0.001
a_3 [1/cm]	0.023	0.003	0.021	0.0005
n_3 [-]	2.85	0.537	4.33	0.139
K_{s3} [cm/min]	68.73	19.7	93.2	3.172
$\theta_{s,im3}$ [-]	-	-	0.35	0
ω_3 [1/min]	-	-	0.00017	0.000003
θ_{s4} [-]	0.01	0.002	0.001	0.00003
a_4 [1/cm]	0.27	0.018	0.247	0.004
n_4 [-]	2.41	0.121	2.17	0.039
K_{s4} [cm/min]	96.7	9.2	56.3	1.051
$\theta_{s,im4}$ [-]	-	-	0.288	0
ω_4 [1/min]	-	-	0.0013	0.00002

1059 Table 9. Confidence intervals (CI) for optimized parameters for both scenarios.

1060

Highlights

- Among Low Impact Development techniques permeable pavement are those that most lacks reliable and accurate modeling tools.
- A mechanistic model is used for the analysis of the hydraulic behavior of a permeable pavement.
- A Global Sensitivity Analysis is used to identify the main effect and interactions of soil hydraulic parameters.
- The model is calibrated by using the metaheuristic Particle Swarm Optimization algorithm.
- The calibrated model is validated on an independent set of measurements with optimal results.